analytical chemistry

pubs.acs.org/ac Article

Simultaneous Recognition of Over- and Under-Expressed MicroRNAs Using Nanopore Decoding

Sotaro Takiguchi, Fumika Kambara, Mika Tani, Tsuyoshi Sugiura, and Ryuji Kawano*

Cite This: https://doi.org/10.1021/acs.analchem.3c02560 Read Online

ACCESS | Metrics & More | Article Recommendations | Supporting Information

ABSTRACT: This paper describes a strategy for simultaneous recognition of over- and under-expressed microRNAs (miRNAs) using the method of signal classification-based nanopore decoding. MiRNA has attracted attention as a promising biomarker for cancer diagnosis owing to its cancer-type-specific expression patterns. While nanopore technology has emerged as a simple and label-free method to detect miRNAs and their expression patterns, recognizing patterns involving simultaneous over/under-expression is still challenging due to the inherent working principles. Here, inspired by the sequence design for DNA computation with nanopore decoding, we designed diagnostic DNA probes targeting two individual over/under-expressed miRNAs in the serum of oral squamous cell carcinoma. Through nanopore measurements, our designed probes exhibited characteristic current signals depending on the hybridized miRNA species, which were plotted on the scatter plot of duration versus current blocking ratio. The classified signals reflected the relative abundance of target miRNAs, thereby enabling successful pattern recognition of over/under-expressed miRNAs, even when using clinical samples. We believe that our method paves the way for miRNA-targeting simple diagnosis as a liquid biopsy.

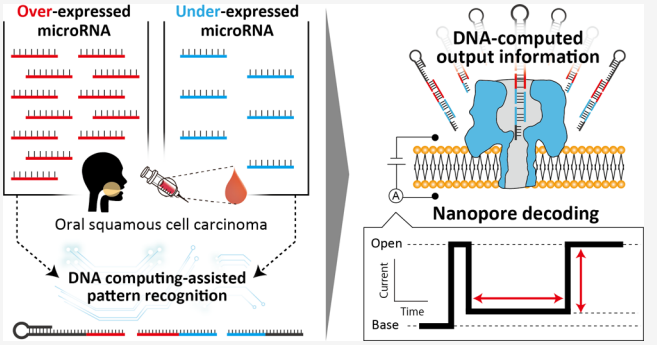

Owing to the high programmability of nucleic acid base-pairing, DNA computing has emerged as a prominent form of molecular computation in wet environments. The initial methodology was proposed in Adleman's pioneering work, with a demonstration using DNA molecules to solve a directed Hamiltonian path problem (HPP),[1] which is mathematically classified as NP-complete and known as the traveling salesman problem. In his work, based on partially complementary hybridization, the "nodes" and "paths" were associated with oligonucleotides to generate routes in a directed graph (Figure 1a), successfully implementing massively parallel computation to solve the HPP. Following this groundbreaking demonstration, extensive studies have been reported using DNA/RNA molecules to implement mathematical models including parallel computation,[2] automaton construction,[3,4] and logic-gate operation.[5,6] In addition to such mathematical modeling, DNA computing has recently expanded the field of research to medical applications due to the advantage of biocompatibility and programmability of nucleic acid molecules.[7] Biological oligonucleotides such as mRNA or miRNA are promising biomarkers in medical diagnosis owing to their potential as input information in DNA computation.[8,9] As described above, DNA computing is attractive as a technology with a wide range of applications, but the output information is encoded in DNA/RNA molecules which then need to be decoded into a human-recognizable signal. Conventional decoding approaches require multistep procedures or fluorescence detection; therefore, a simple decoding method has been in demand.

Nanopore technology is a promising tool for the electrical and label-free detection of oligonucleotides.[10−13] Especially, α-hemolysin (αHL), a pore-forming membrane protein from *Staphylococcus aureus*,[10] is conventionally used for oligonucleotide detection due to the size compatibility between the pore and single-stranded DNA. This size compatibility allows electrical discrimination of not only four individual nucleobases[12] but also nucleic acid structures (single-stranded (ss), double-stranded (ds), and other higher-order structures).[14,15] The results of DNA computation are output as DNA/RNA molecules, leading us to design the DNA-computed output information via nucleic acid structural information. Combining this structural design with αHL nanopore technology, we have developed a nanopore-based decoding method in DNA computation.[16] We first constructed a simple DNA logic gate with output 0/1 information encoded as ss/dsDNA, which resulted in transient/long-time current blocking signals which were

Received: June 13, 2023
Accepted: August 28, 2023

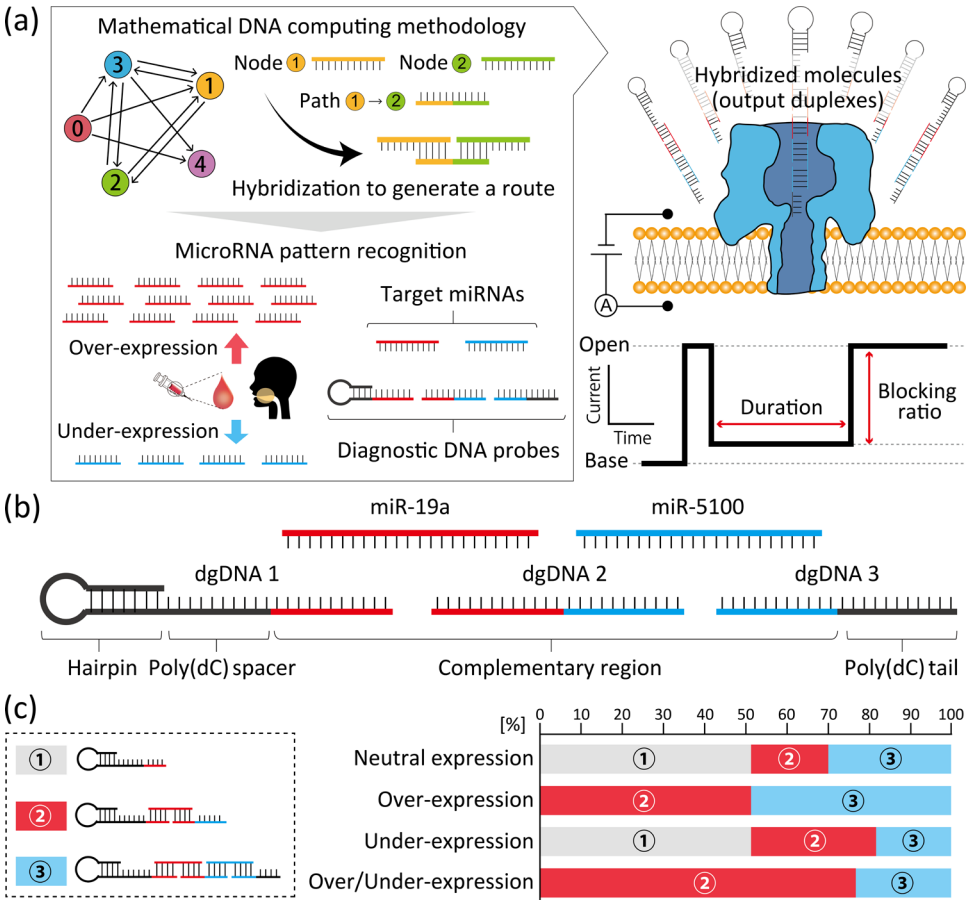

Figure 1. (a) Sequence design principle of diagnostic DNA probes (dgDNAs) inspired by mathematical DNA computation for the simultaneous pattern recognition of OSCC-related over/under-expressed miRNAs with nanopore-derived current signal analysis. (b) Design of diagnostic DNAs. (c) Illustration of the three types of the output duplex structures; output 1 (dgDNA 1), output 2 (dgDNA 1 + miR-19a + dgDNA 2), and output 3 (dgDNA 1 + miR-19a + dgDNA 2 + miR-5100 + dgDNA 3). Bar graphs show the abundance ratio of the three types of output duplex as the results of thermodynamic simulations. The abundance ratios of output 1, output 2, and output 3 were, respectively, calculated to be 51, 19, and 30% for the neutral expression pattern, 0, 51, and 49% for the over-expression pattern, 51, 32, and 17% for the under-expression pattern, and 0, 76, and 24% for the over- and under-expression pattern.

successfully decoded through nanopore measurement.[17] Subsequently, a logic network[18] and an enzyme-involved complex logic operation[19] were also constructed using the droplet-based nanopore system. In addition, by designing the ΔG of the output duplex, we were able to decode Adleman's DNA-based parallel computation, the DNA-encoded HPP, utilizing the duration of the current blocking signals as the decoding parameter.[20] To that end, the method of nanopore decoding has been developed as a powerful tool for direct and simple decoding within diverse DNA computations; the next phase of our research endeavor is toward medical applications. Our target miRNA, a short noncoding RNA of 18-25 nucleotides, is a promising biomarker for cancer diagnosis because over/under-expression patterns of miRNAs in bodily fluids show cancer type specificity.[21,22] As a strategy for miRNA expression pattern recognition, we have used DNA computation methodology to design probes that bind to miRNAs. In this approach, the designed probes perform hybridization-based molecular computation with the target miRNAs, and the output hybridized duplexes reflect the information of the miRNA expression pattern, which is then detected and decoded through nanopore measurement. Initially, we constructed an AND gate using two over-expressed miRNAs from small-cell lung cancer as inputs.[23] In this system, the expression pattern of miRNAs was described as an AND logic operation, resulting in the formation of a four-way junction with designed diagnostic DNA probes only in the case of input (1, 1). The method of nanopore decoding was able to discriminate the AND operations depending on the structural change of output molecules, with discrimination of miRNA expression patterns. Moreover, Takeuchi et al. have recently reported that a target-sequence-encoded diagnostic DNA probe was able to perform parallel detection of five miRNAs, which was reported to be over-expressed in bile duct cancer (BDC) patients,[24] using pattern recognition.[25] Using this method, we achieved the discrimination of plasma miRNA expression patterns between BDC patients and healthy volunteers. Consequently, based on the principle of the increase in current blockage duration with increasing miRNA concentration, we successfully demonstrated the pattern recognition of multiple over-expressed miRNAs using DNA computation methodology and nanopore decoding. However, the recognition of simultaneous over/under-expression patterns is still challenging because the working principle of the nanopore decoding method depended on the single decoding parameter: the current blockage duration, which increased upon the hybridization with target miRNAs.

In this study, we report the method for pattern recognition of two individual over/under-expressed miRNAs with current signal classification-based nanopore decoding using diagnostic

https://doi.org/10.1021/acs.analchem.3c02560
Anal. Chem. XXXX, XXX, XXX−XXX

DNA probes (dgDNAs), whose design is inspired by our previous mathematical DNA computation[20] (Figure 1a). Target miRNAs show aberrant expression (over-expression; miR-19a, under-expression; miR-5100) in the serum of oral squamous cell carcinoma (OSCC) patients, which is one of the most common cancers worldwide.[26] Toward simultaneous pattern recognition of over/under-expressed miRNAs, we here utilize DNA-based parallel computation methodology to design dgDNAs. In this method, as a result of molecular computation by dgDNAs and miRNAs, three types of duplexes were generated depending on the hybridized miRNA species, with their specific abundance ratio reflecting the relative abundance of miRNAs. Through nanopore measurements, the output duplexes exhibited characteristic current signals, which were plotted on the scatter plot of duration versus current blocking ratio. We were able to decode information on the relative abundance of target miRNAs from the classified signals on the scatter plot, thereby enabling successful pattern recognition of the OSCC-specific over/under-expressed miRNAs, even when using clinical samples.

EXPERIMENTAL SECTION

Reagents and Chemicals. In this study, we used the following reagents: 1,2-diphytanoyl-*sn*-glycero-3-phosphocholine (DPhPC; Avanti. Polar Lipids, Alabaster, Alabama), *n*-decane (Wako Pure Chemical Industries, Ltd., Osaka, Japan), potassium chloride (KCl; Nacalai Tesque), 3-morpholinopropane-1-sulfonic acid (MOPS; Nacalai Tesque, Kyoto, Japan). Buffered electrolyte solutions (1 M KCl, 10 mM MOPS, pH 7.0) were prepared using ultrapure water, which was obtained from a Milli-Q system (Millipore, Billerica, Massachusetts). Wild-type α-hemolysin (αHL; Sigma-Aldrich, St. Louis, Missouri) was obtained as the monomer polypeptide, isolated from *Staphylococcus aureus* in the form of a powder and dissolved at a concentration of 1 mg/mL in ultrapure water. For use, samples were diluted to the designated concentration using a buffered electrolyte solution and stored at 4 °C. HPLC-grade DNA, RNA, and LNA-inserted DNA oligonucleotides were synthesized by Eurofins Genomics Inc. (Tokyo, Japan), FASMAC Co., Ltd. (Kanagawa, Japan), and GeneDesign, Inc. (Osaka, Japan), respectively, stored at −20 °C. 10× TBE buffer was obtained from Takara Bio Inc. (Shiga, Japan) and was 10-fold diluted for gel electrophoresis. The power supply and an LED transilluminator were obtained from Bio Craft Co., Ltd. (Tokyo, Japan) and ATTO Co., Ltd. (Tokyo, Japan), respectively.

DNA Design and Thermodynamic Simulation. To confirm the hybridization and to simulate the DNA computation, thermodynamic simulations were performed using the NUPACK webserver (California Institute of Technology, http://www.nupack.org/). These analyses were performed under the condition of 1 M KCl at 22 °C. The concentrations of dgDNAs and neutral expression levels of miRNAs were set to 500 and 250 nM, respectively. In the case of over- or under-expression, the concentrations of miRNAs were set to be 500 nM (2-fold) and 125 nM (0.5-fold), respectively.

Native Polyacrylamide Gel Electrophoresis. The duplex formation was confirmed by native PAGE using 10% gels (29:1 acrylamide/bis (w/w)) in 1 × TBE buffer at a constant power of 1.0 W for 120 min at 4 °C. After electrophoresis, the gel was stained with diluted SYBR Green II solution (Takara Bio Inc.) for 30 min and visualized under blue LED irradiation. Images were obtained using LuminoGraph I (ATTO Co., Ltd., Tokyo, Japan).

Preparation of the Microdevice. Microdevices were fabricated by machining a 6.0 mm thick, 10 mm × 10 mm poly(methyl methacrylate) (PMMA) plate (Mitsubishi Rayon, Tokyo, Japan) using computer-aided design and manufacturing with a three-dimensional modeling machine (MM-100, Modia Systems, Japan) as shown in Figure S1b−d. Two wells (2.0 mm diameter and 4.5 mm depth) and a chase between the wells were manufactured on the PMMA plate. Each well had a through-hole in the bottom and Ag/AgCl electrodes were set into this hole. A polymeric film made of parylene C (polychloro-*p*-xylylene) with a thickness of 5 μm was patterned with a single pore (100 μm diameter) using a conventional photolithography method and then fixed between PMMA films (0.2 mm thick). The films, including the parylene film, were inserted into the chase to separate the wells and fixed using an adhesive bond (Acrysunday Co., Ltd., Tokyo, Japan).

Lipid Bilayer Preparation, Channel Current Recording, and Data Analysis. Lipid bilayers were prepared in the microdevice using the droplet contact method[20,27,28] (Figure S1a), as described in the following procedures: the wells of the device were filled with *n*-decane (0.8 μL) containing DPhPC (10 mg/mL). The buffered solution (4.7 μL) with αHL (final concentration 30 nM) and oligonucleotides were poured into one chamber which was connected to the ground terminal. The buffered solution (4.7 μL) was also poured into another chamber which was connected to the recoding terminal. In this study, the buffered solution (1 M KCl, 10 mM MOPS, pH 7.0) was used for each droplet. Within a few minutes of adding the solutions, a lipid bilayer formed on a parylene C film that separates the two chambers, and αHL formed a nanopore by reconstitution in the lipid bilayer. When the lipid bilayers ruptured during this process, they were reassembled by tracing with a hydrophobic stick at the droplet interface. The channel current was recorded with an Axopatch 200B amplifier (Molecular Devices), filtered with a low-pass Bessel filter at 10 kHz at a sampling rate of 50 kHz. A constant voltage of +120 mV was applied from the recording side, and the ground side was grounded. In the event that DNA/RNA molecules become clogged within the nanopore, resulting in a prolonged current blocking duration exceeding our predefined threshold of 25 000 ms, we employed a transient voltage inversion to eject the obstructing molecule from the nanopore. This procedure allows the continued detection of other molecules. The recorded data from Axopatch 200B was acquired with Clampex 11.2 software (Molecular Devices) through a Digidata 1440A analog-to-digital converter (Molecular Devices). Data were analyzed using Clampfit 11.2 (Molecular Devices), Excel (Microsoft, Washington), Origin pro 8.5J (Light Stone, Tokyo, Japan), and Python (Python Software Foundation, Delaware). The analyzed data were obtained from at least three different αHL nanopores. Oligonucleotides were detected when > 48% of open αHL channel currents were inhibited.[14] The duration time of blocking signals was filtered between 300 μs and 25 000 ms. 300 samples were randomly extracted from all data to produce the scatter plots of duration versus current blocking ratio. These data sampling and analysis are described in detail in the Supporting Information. The 95% CI of the experimentally obtained abundance ratio (bar graph) was calculated using the following equation:

$$\bar{p} - 1.96\sqrt{\bar{p}(1-\bar{p})/n} \le p \le \bar{p} + 1.96\sqrt{\bar{p}(1-\bar{p})/n}$$

https://doi.org/10.1021/acs.analchem.3c02560
Anal. Chem. XXXX, XXX, XXX−XXX

Table 1. Oligonucleotides Sequences (Underline Indicates the LNA Nucleotides)

	sequence
miR-19a	5′ UGUGCAAAUCUAUGCAAAACUGA 3′
miR-5100	5′ UUCAGAUCCCAGCGGUGCCUCU 3′
dgDNA 1	5′ GTAGAACTTTTGTTCTACCCCCCCCCCCCCTCAGTTTTGCA 3′
dgDNA 2	5′ TAGATTTGCACAAGAGGCACCGC 3′
dgDNA 3	5′ TGGGATCTGAACCCCCCCCCC 3′

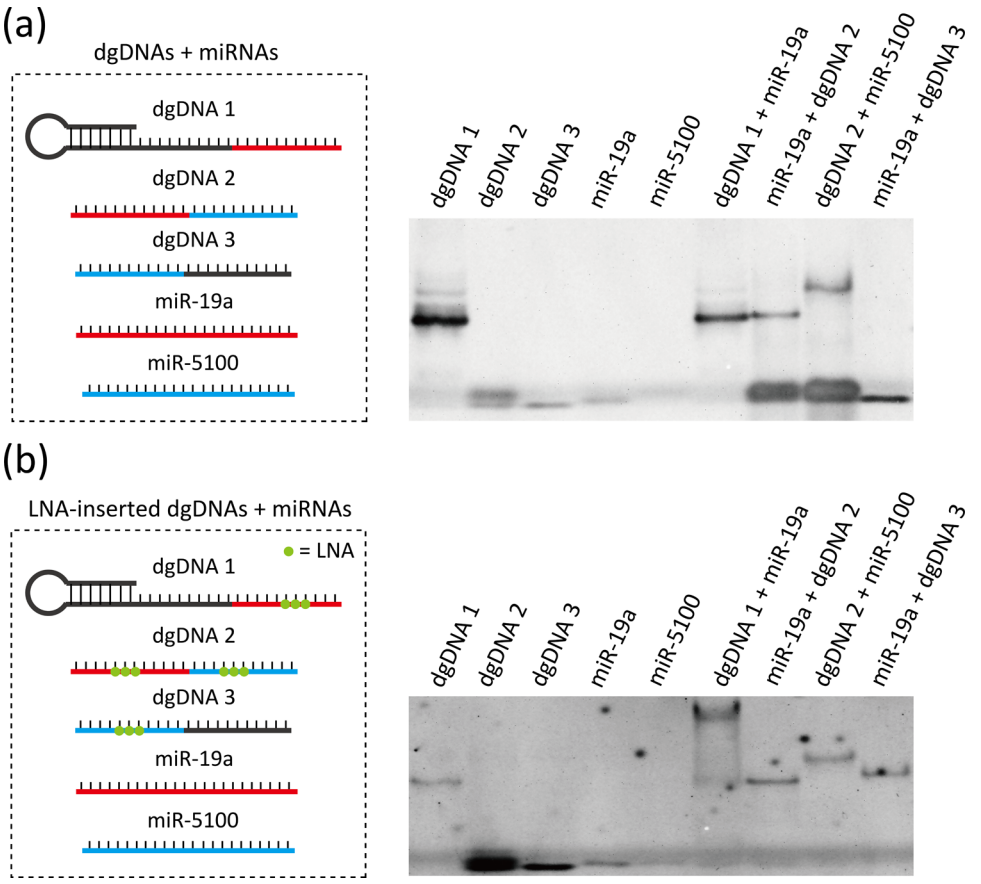

Figure 2. Native PAGE to confirm the duplex formation between (a) dgDNAs and miRNAs and (b) LNA-inserted dgDNAs and miRNAs.

where $\bar{p}$ is the sample ratio, p is the population ratio, and n is the sample number.

Reference Data Preparation and Nanopore Decoding for miRNA Pattern. To obtain the reference data, each output duplex was prepared at the final concentration of 1 μM by the following procedure. Each solution contained 1 μM oligonucleotides, 1 M KCl, and 10 mM MOPS (pH 7.0). These solutions were heated to 95 °C for 5 min and then cooled to room temperature gradually. To prepare four types of miRNA expression pattern solutions, each oligonucleotide was added (1 M KCl, and 10 mM MOPS (pH 7.0)) to a designated concentration, which is the same as the condition of the simulation, in a buffered solution. These solutions were also heated to 95 °C for 5 min and then cooled to room temperature gradually. In the case of low concentrations of oligonucleotides, the concentration of dgDNAs and miRNAs was designated to be 50 and 25 pM, respectively. The 50 pM concentration for dgDNA was also used when using clinical samples.

Small RNA Extraction and Quantification of miRNA by RT-qPCR. Small RNAs were extracted from 300 μL of each serum sample using the NucleoSpin miRNA Plasma (Takara Bio, Inc., Shiga, Japan) according to the manufacturer's protocol. Eluted solutions with a final volume of 30 μL were stored at −80 °C until used. MiRNA concentrations were quantified by reverse transcription quantitative PCR (RT-qPCR) using the Mir-X miRNA qRT-PCR TB Green Kit (Takara). Reverse transcription was performed using the Mir-X miRNA First-Strand Synthesis Kit (Takara) according to the manufacturer's protocol. Quantitative PCR was performed using the Thermal Cycler Dice Real-Time System Lite (Takara) with the following procedure: the reaction mixtures were incubated at 95 °C for 10 s, followed by 40 cycles at 95 °C for 5 s and 65 °C for 25 s. Cycle threshold (Ct) values were calculated using Multiplate RQ (Takara).

RESULTS AND DISCUSSION

Design of Diagnostic DNA Probes and Simulated Results of DNA Computation. We selected miR-19a and miR-5100 as targets because these miRNAs have been reported to be respectively over/under-expressed in the serum of human OSCC patients. According to the quantitative analysis, the over- (miR-19a) and under- (miR-5100) expression level was determined to be 2- and 0.5-fold, respectively.[29] Toward

https://doi.org/10.1021/acs.analchem.3c02560
Anal. Chem. XXXX, XXX, XXX−XXX

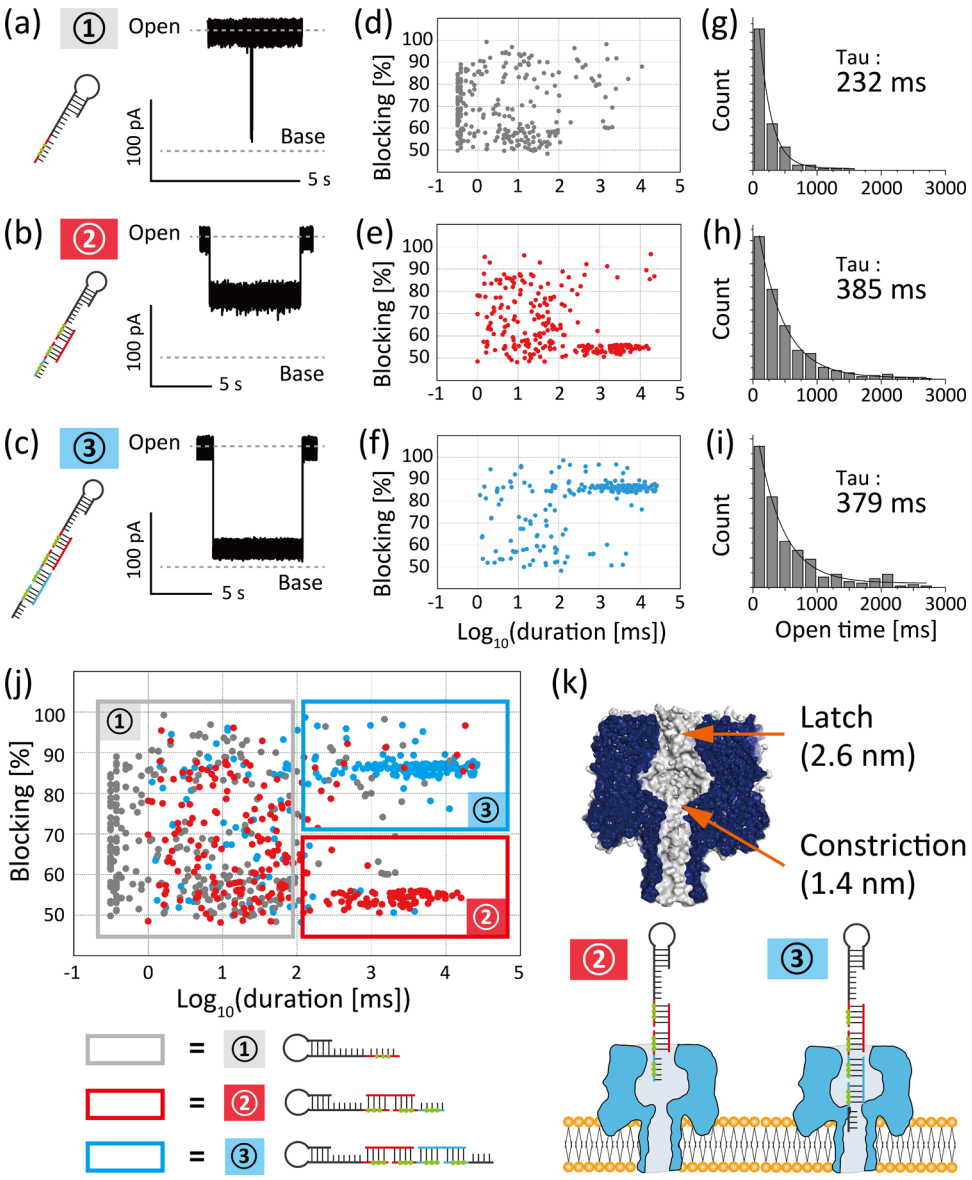

Figure 3. Typical current blocking signals of (a) output 1, (b) output 2, and (c) output 3. (d–f) Scatter plots of duration versus the current blocking ratio of (d) output 1 (e) output 2, and (f) output 3. (g–i) Analysis of the frequency of the blocking signals reflecting the detection of (g) output 1, (h) output 2, and (i) output 3. (j) Merged scatter plot as a reference data for nanopore decoding. Each surrounded area which reflected the detection signal of each output duplex was defined as follows; output 1: 300 μs < duration $\leq$ 100 ms, 48% $\leq$ blocking, output 2: 100 ms < duration < 25 000 ms, 48% $\leq$ blocking < 70%, output 3: 100 ms < duration < 25 000 ms, 70% $\leq$ blocking. (k) Structure of αHL (PDB ID: 7AHL) and the proposed models for the clogging of output 2 (latch) and output 3 (constriction) in the αHL nanopore.

simultaneous pattern recognition of these miRNAs, we here utilized sequence design for DNA-based parallel computation[1,20] and designed dgDNAs, which consisted of a partially complementary sequence with target miRNAs (Figure 1b). As a proof of concept, four expression patterns of target miRNAs were prepared involving over/under-expression, and we thermodynamically simulated the molecular computation using nanomolar concentrations of oligonucleotides (described in detail in the Experimental Section). As a result, depending on the hybridized miRNA species, three types of duplexes (output 1–3) were generated in all patterns, and their abundance ratio allowed us to distinguish the four miRNA expression patterns (Figure 1c). The relative abundance of the output duplexes is correlated with their concentration, which is validated as the individual frequency of the current blocking event in nanopore measurements.[30] Therefore, this output information can be decoded by nanopore-based identification of the output duplexes. The sequences of the designed dgDNAs are listed in Table 1, and the structural design strategies are as follows:

(1) Poly(dC) is added at the 3′ end of dgDNA 3 for insertion into the αHL nanopore from the 3′ terminus of the output duplexes. The 3′ single-stranded tail structure has been reported to be highly efficient in the generation of current blocking events.[31]

(2) The current blocking duration changes drastically depending on the 5′/3′ direction of the nucleic acids for insertion into the nanopore.[28] To enhance the target specificity of the current blocking signals, a hairpin structure is added to the 5′ end of dgDNA 1 to restrict the translocation direction of the output duplexes through the αHL nanopore.[32]

https://doi.org/10.1021/acs.analchem.3c02560
Anal. Chem. XXXX, XXX, XXX−XXX

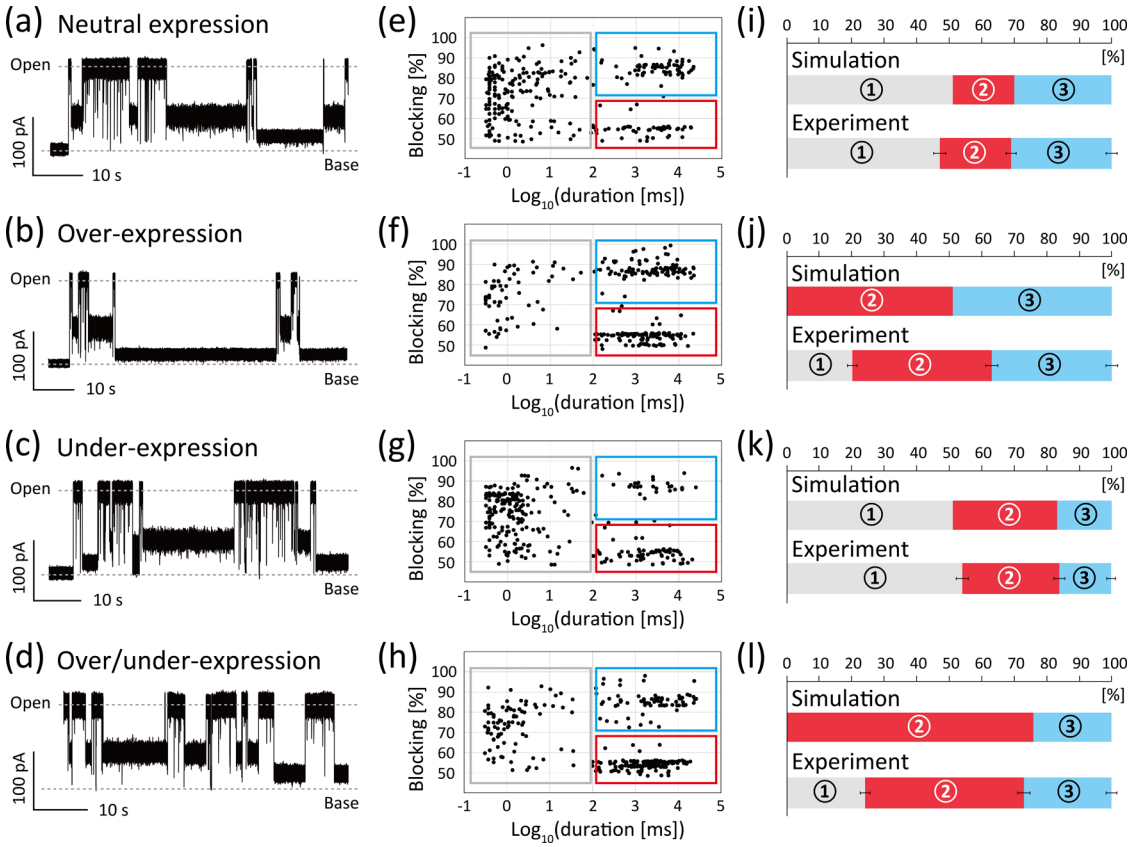

Figure 4. Results of nanopore decoding using the miRNA pattern solution of (a, e, i) neutral expression, (b, f, j) over-expression, (c, g, k) under-expression, and (d, h, l) over- and under-expression. (a−d) Typical current−time traces, (e−h) scatter plots of duration versus current blocking ratio, and (i−l) the comparison of the abundance ratio between simulation results and experimental results. Error bars represent the 95% CIs.

(3) A poly(dC) spacer is added between the hairpin structure and dgDNA 1/miR-19a binding region to form A-type (DNA-RNA) and B-type (DNA−DNA) duplexes simultaneously.[33]

First, we experimentally confirmed the duplex formation between dgDNAs and miRNAs using native PAGE. Figure 2a shows the results for each binding site, in which bands of unhybridized oligonucleotides were mainly observed, probably owing to the short nucleotide length for hybridization. Facilitating the duplex formation by introducing locked nucleic acids (LNA)[34,35] into dgDNAs (the insertion position is listed in Table 1), we successfully confirmed the dgDNAs/miRNAs binding as shown in Figure 2b (additional confirmation is shown in Figure S3). LNA-inserted probes have been reported to have a target specificity at the single-base level in nanopore measurement.[36,37] By investigating the miRNA database,[38] we found that our target miR-19a has the family sequence as SNPs, but the designed dgDNAs have enough specificity to recognize the target miRNA in a variety of sequence contexts by the LNA insertion.

Preparation of the Reference Data for Nanopore Decoding. As mentioned above, the strategy of nanopore decoding is premised on identifying the three types of output duplexes. Therefore, we subsequently investigated the current blocking signals of each duplex in nanopore measurements. Figure 3a−c shows the representative current blocking signals of each output duplex. In the scatter plot of duration versus the current blocking ratio of each signal, a specific plotting area appeared in duration > 100 ms and 56% < blocking ratio < 60% in all measurements (Figure S4c−e). These plots were experimentally assigned to the clogging of duplexes in the αHL nanopore from their hairpin terminus, by using dumbbell-shaped DNA and hairpin-less output molecule (Figures S4 and S5, the sequence is listed in Table S1). Filtering the hairpin clogging signals, we obtained the reference scatter plot of each output duplex as shown in Figure 3d−f. The merged plot suggested that the three types of duplexes were distinguishable from the current blocking signals in nanopore measurements and the plots can be classified into the framed area corresponding to each output duplex (Figure 3j). The difference in the blocking ratio between output 2 and output 3 was considered to reflect their structural difference. Regarding the length of the single-stranded tail, which has been reported to influence the current blocking ratio,[39] it was the same between output 2 and output 3. As another factor, Perera et al. reported that the helical form-dependent duplex diameter significantly influenced the current blocking ratio.[14] According to their results, A-form duplexes with a larger diameter (=2.4 nm) clogged at the latch of αHL (Figure 3k), resulting in a shallow current blockage (around 50% blocking). In contrast, B-form duplexes with a smaller diameter (=2.0 nm) clogged at the constriction of αHL (Figure 3k), resulting in a deep current blockage (approximately 85% blocking). Referring to this report,[14] our output 2 and output 3 clogged αHL at the latch and constriction, respectively, probably as a sequence-dependent phenomenon (investigated in detail in Figure S6), allowing for discrimination via the current blocking ratio (Figure 3k). Using the framed area corresponding to the output duplexes, we calculated the false positive rates as follows: 13% for output 2

https://doi.org/10.1021/acs.analchem.3c02560
Anal. Chem. XXXX, XXX, XXX−XXX

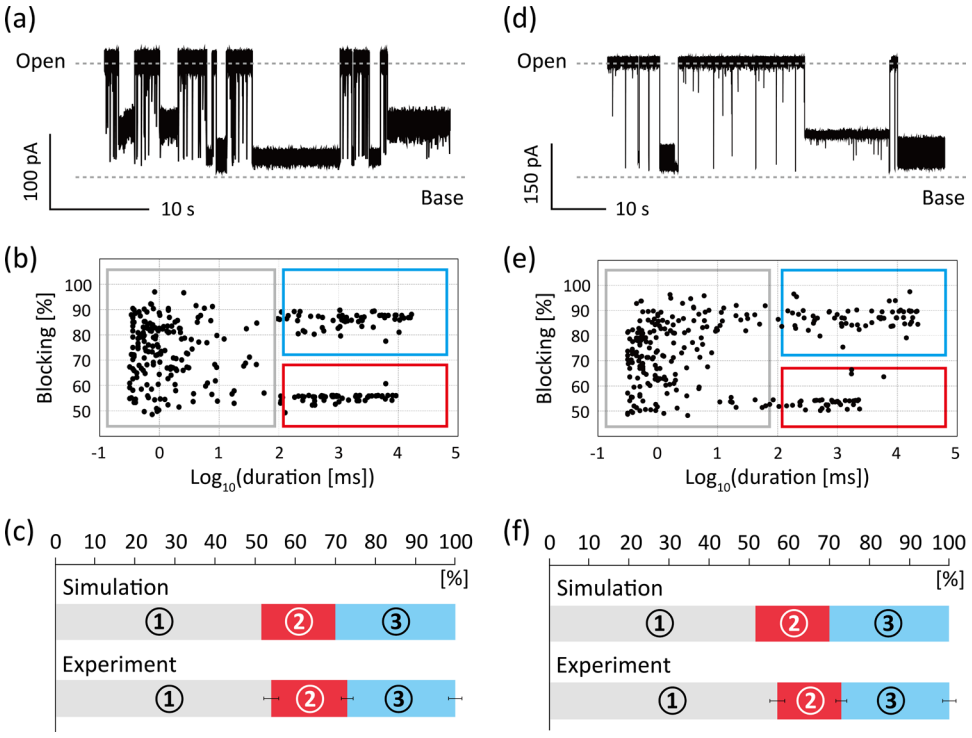

Figure 5. Results of nanopore decoding using neutral expression pattern solution (a–c) with nontarget miRNA and (d–f) at a low concentration. (a, d) Typical current–time traces, (b, e) scatter plots of duration versus current blocking ratio, and (c, f) the comparison of the abundance ratio between simulation results and experimental results. Error bars represent the 95% CIs.

identified as output 1, 9% for output 3 identified as output 1, 2% for output 1 identified as output 2, 2% for output 3 identified as output 2, 4% for output 1 identified as output 3, and 3% for output 2 identified as output 3. In the range of 1 ms < duration < 100 ms, which exhibited the highest level of overlap, we assigned these signals in output 2 and output 3 measurements to the detection of output 1 as unbound molecules to calibrate misidentification. With this reference scatter plot and framed area assignment, we next implemented nanopore decoding using the four types of pseudo-miRNA expression pattern solutions.

Nanopore Decoding for the Four Expression Patterns of miRNAs. The four series of pseudo-miRNA pattern solutions were prepared using nanomolar concentrations of oligonucleotides, which were synonymous with the simulation conditions (described in detail in the Experimental Section). In the nanopore measurements, several types of current-blocking signals were observed as shown in Figure 4a–d. Producing the scatter plots of duration versus blocking ratio (Figure 4e–h), we assigned each plot to each output duplex based on the reference data and framed area assignment (Figure 3j). For calculating the abundance ratio of the three types of output duplexes, we counted the number of plots within each framed area in the graph. To calibrate both the false positives of the misidentifications of the output molecules (overlap in Figure 3j) and their differences in the frequency to be captured into nanopore, we used the frequency values of the current blocking events derived from each output molecule (Figures 3g–i and S7). Following the above data analysis as described in detail in the Supporting Information, the abundance ratio of output 1, output 2, and output 3 were, respectively, calculated to be 47 ± 6, 22 ± 5, and 31 ± 5% for the neutral expression pattern (Figure 4i), 20 ± 5, 43 ± 6, and 37 ± 6% for the over-expression pattern (Figure 4j), 54 ± 6, 30 ± 5, and 16 ± 4% for the under-expression pattern (Figure 4k), 21 ± 5, 52 ± 6, and 27 ± 5% for the over/under-expression pattern (Figure 4l). The calculated abundance ratio of the output duplexes within each pattern was significantly different except for the case between output 2 and 3 in the over-expression pattern (Figure 4j) and between output 1 and 3 in the over/under-expression pattern (Figure 4l). Regarding the percentage order, the experimentally obtained abundance ratio was consistent with simulation results, discriminating the four expression patterns of miRNA involving over/under-expression. Although the output 1 signals appeared in the over-expression pattern (Figure 4j) and the over- and under-expression pattern (Figure 4l), it was negligible when comparing the percentage order with simulation results. Consequently, our proposed method successfully demonstrated the simultaneous monitoring of over/under-expression patterns of target miRNAs.

Confirmation of the Target Specificity. Although LNA-inserted probes have been reported to have single-base resolution specificity,[36,37] we experimentally confirmed the target specificity of our proposed method by adding a nontarget miRNA (the sequence is listed in Table S1) to a pseudo-neutral expression pattern solution at the same concentration as the target miRNAs. As shown in Figure 5a, several types of blocking signals were observed in nanopore measurements. Producing a scatter plot of duration versus blocking ratio (Figure 5b), we assigned each plot to each output duplex based on the reference data. As a result, the abundance ratio of output 1, output 2, and output 3 was calculated to be 54 ± 6, 19 ± 4, and 27 ± 5%, respectively, with these values being significantly different. In terms of the percentage order, the experimentally obtained abundance ratio was consistent with the simulation result (Figure 5c), showing the target specificity of our method. Although the event frequency of blocking signals with duration <300 μs, which reflects the translocation of short single-stranded

https://doi.org/10.1021/acs.analchem.3c02560
Anal. Chem. XXXX, XXX, XXX–XXX

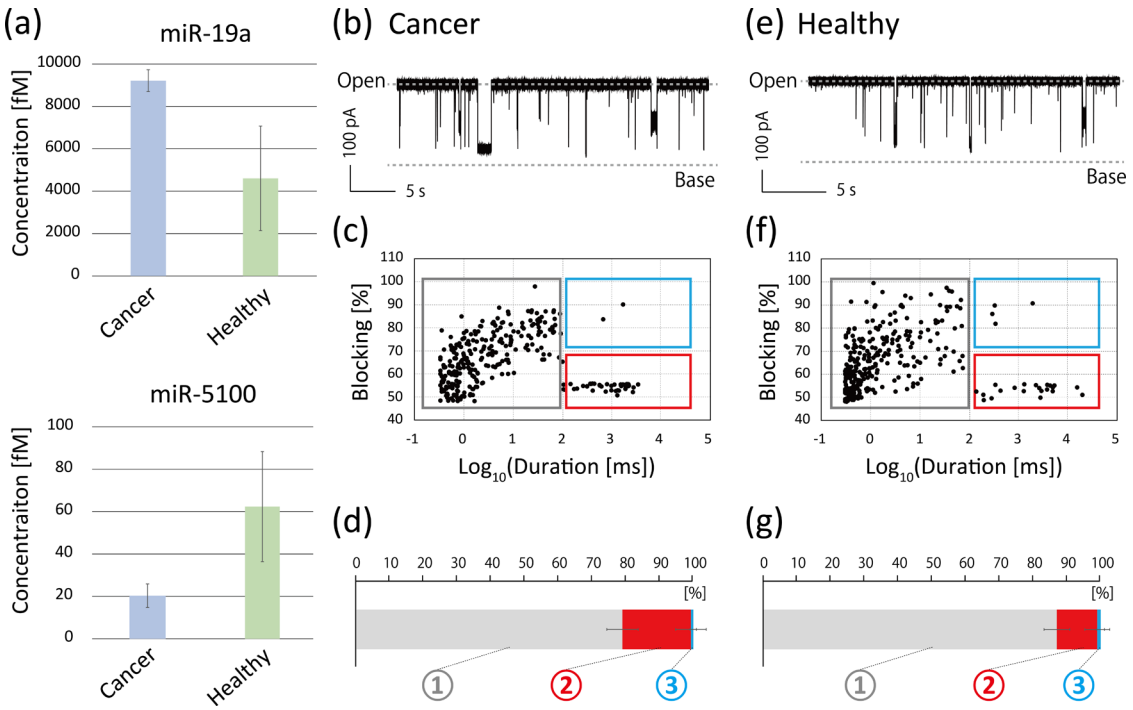

Figure 6. (a) MiRNA concentrations in pooled samples (=averages) of the three cancer patient samples with spiked-in miR-19a and the three healthy volunteer samples. (b–g) Results of nanopore decoding using (b–d) pooled cancer sample with spiked-in miR-19a and (e–g) pooled healthy sample. (b, e) Typical current–time traces, (c, f) scatter plots of duration versus current blocking ratio, and (d, g) experimentally obtained abundance ratio. Error bars represent the 95% CIs.

oligonucleotides,[40,41] were indeed increased by adding the nontarget miRNA (Figure S9), such signals were filtered through data analysis.

Estimation of the Durability against the Low miRNA Concentration and against the Range of Concentration Change. Considering diagnostic applications, we next confirmed the durability of our proposed method against low concentrations of oligonucleotides using a picomolar pseudo-neutral expression pattern solution (described in detail in the Experimental Section). In nanopore measurements, the frequency of the current blocking event drastically decreased with a reduction in oligonucleotide concentration, leading us to adopt asymmetric conditions to enhance the event frequency (Figure S10).[31,42] As shown in Figure 5d, several types of blocking signals were observed even with asymmetric conditions. Producing a scatter plot of duration versus blocking ratio (Figure 5e), we assigned each plot to each output duplex based on the reference data. As a result, the abundance ratio of output 1, output 2, and output 3 was calculated to be 57 ± 6, 16 ± 4, and 27 ± 5%, respectively, with these values being significantly different. In terms of percentage order, the experimentally obtained abundance ratio was consistent with the simulation result (Figure 5f), showing the durability of this system for low miRNA concentrations as secreted in bodily fluids.

In this study, the over/under-expression levels of target miRNAs were set to be 2- and 0.5-fold, respectively. We here discuss the durability of our proposed method against a range of miRNA concentration changes using thermodynamic simulations. As shown in Figure S11, in the case of 2-, 5-, and 10-fold over-expression, the abundance ratio of the three types of duplexes drastically changed depending on the expression level. The differences in abundance ratio could be distinguished in nanopore measurements, indicating that this method is potentially robust against over-expressed miRNA recognition. On the other hand, in the case of 0.5-, 0.2-, and 0.1-fold under-expression, there were slighter differences in the simulated abundance ratio compared with the over-expression simulations. Especially in the case of 0.1-fold under-expression, the abundance ratio of output 3 was calculated to be <0.1%, which is considered to be difficult to detect and to calculate the abundance ratio by nanopore measurements. In summary, as a limitation of this method, the cancer-derived concentration change of miRNAs should exceed a minimum threshold of 0.1-fold. To overcome the above limitation in detecting the under-expressed miRNA, probe design is one of the effective strategies, which enhances the event frequency of a specific output molecule that shows less than 0.1-fold under-expression.[31,39] When employing this method over a wide range of miRNA concentration changes, the simulated data indicated that the identification of the four expression patterns (shown in Figure 3) was challenging due to the unchanged percentage order of the output duplexes (Figure S11). However, the trends of cancer-derived simultaneous over/under-expression of miRNAs appeared in the abundance ratio as an increase in output 2 coupled with a decrease in output 3 compared to the neutral expression pattern. By capturing this change in the relative abundance of the output duplexes, our method potentially performs simultaneous recognition of over/under-expressed miRNAs.

Operational Confirmation Using Clinical Samples. Our targeting miR-19a and miR-5100 have been reported to be 2-fold over-expressed and 0.5-fold under-expressed, respectively, in the serum of human OSCC patients.[29] Since the collected serum samples from OSCC patients (N = 3) and healthy volunteers (N = 3) had the same clinicopathological background

https://doi.org/10.1021/acs.analchem.3c02560
Anal. Chem. XXXX, XXX, XXX−XXX

as in the previous report,[29] we first attempted nanopore measurement using pooled samples containing miRNAs extracted from the serum samples. Employing the asymmetric electrolyte conditions, three types of output duplex-detection signals were observed even when using clinical samples (Figure S12). The signals could be classified based on the reference data; however, the experimentally obtained abundance ratio of the output duplexes conflicted with the miRNA profiling trends in the previous report;[29] our data indicated under-expression of both miR-19a and miR-5100 in OSCC patients (Figure S12). To validate the expression level of miR-19a and miR-5100, we performed absolute quantification of target miRNAs in the individual serum samples using RT-qPCR (calibration curve preparation is shown in Figure S13). Comparing the average values, the cancer-induced concentration changes were calculated to be 0.2-fold for miR-19a and 0.3-fold for miR-5100 (Figure S14, miRNA concentrations in individual samples are listed in Table S2), which profile differed from the previous report[29] but was consistent with our nanopore analysis result. Although the relative abundance of target miRNAs was able to be detected using pooled samples, we decided to introduce a spike-in of miR-19a into the cancer pool to model the scenario of 2-fold over-expression (Figure 6a). Even with the spike-in clinical sample, several types of blocking signals were observed (Figure 6b,e), which were successfully classified on the scatter plot of duration versus blocking ratio (Figure 6c,f). Based on the reference data and framed area assignment, the abundance ratio of output 1, output 2, and output 3 was calculated to be 79 ± 5, 20 ± 5, and 0.7 ± 1% (these values being significantly different) for the cancer patients pool, and 87 ± 4, 12 ± 4, and 1 ± 1% (these values being significantly different) for the healthy volunteer pool, respectively (Figure 6d,g). The significant trend of an increase in output 2 coupled with a concomitant decrease in output 3, was indicative of the OSCC-induced changes in the relative abundance of target miRNAs (Figure 6d,g). To that end, our method successfully captured the trend of simultaneous over/under-expression at the clinical level.

Finally, we discuss a limitation inherent in this method regarding target selection and the concentration disparities among the target miRNAs. In our proposed method, the detection of output 3 (miR-5100) is dependent on the presence of output 2 (miR-19a) due to the stepwise binding principle among dgDNAs and miRNAs. Therefore, the concentration of miRNA proximity to dgDNA 1 (miR-19a in this study) must be higher than another one next to itself (miR-5100 in this study). Referring to the reported statistical data, careful selection of the target miRNA species is required based on the in-order concentration limitation. We believe that a strategic dgDNA design can address this limitation. By preparing the reference data of all potential hybridization products (outputs) and designing the dgDNAs so that all outputs are distinguishable in the scatter plots, we can assess the relative abundance of target miRNAs independent of their concentration order using our proposed analysis method. Regarding the miRNA concentration disparities, due to the correlation between the miRNA concentration and the event frequency of current-blocking signals, concentration differences between target miRNAs lead to a compression of the experimentally obtained abundance ratio for a specific molecule, as shown in output 3 of our results (Figure 6d,g). To effectively monitor both over/under-expressed miRNAs, the concentration differences between the target miRNAs should be within a range of 500-fold, detectable three types of duplexes simultaneously. One viable strategy to overcome this limitation is to increase the number of targeting miRNAs, thereby mitigating the interference of miRNAs that are secreted at aberrant concentrations compared to others. The design of our dgDNAs can accommodate a larger number of targeting miRNAs, suggesting the potential to achieve resilience to the above limitation.

CONCLUSIONS

In conclusion, we proposed a strategy for the simultaneous pattern recognition of over/under-expressed miRNAs, leveraging custom-designed DNA probes and nanopore-derived current signal classification. Our designed probes, dgDNAs, whose sequence design was inspired by mathematical DNA computation, formed three types of duplexes depending on the hybridized miRNAs as the output of the molecular computation. By subjecting each output duplex to nanopore measurements, we observed distinct current-blocking signals, which were plotted on the scatter plot of duration versus current blocking ratio and successfully classified. The classified signals reflected the relative abundance of the target miRNAs, allowing the four expression patterns of OSCC-related miRNAs involving over/under-expression to be distinguished using pseudo-miRNA pattern solutions. Our data indicated that the proposed method had target specificity, and durability in the face of low oligonucleotide concentrations. Furthermore, this method was able to detect the trend of simultaneous over/under-expression of target miRNAs even when using clinical samples. Simultaneous detection of over/under-expression is generally challenging in other approaches such as surface plasmon resonance,[43] electrochemical sensors,[44] and fluorescence detection.[45] In addition to achieving the over/under-expression recognition, our probe design allows for the accommodation of a larger number of miRNAs, showing the potential for more complex miRNA pattern recognition. With these advantages, we believe that our method provides a powerful tool for miRNA pattern recognition that can be used in simple cancer diagnosis.

In addition, commercially available nanopore devices such as the MinION from Oxford Nanopore Technology have recently attracted attention as a portable and high-throughput platform for nanopore sensing.[46−49] By introducing the oligonucleotide-containing electrolyte solution into the flow cell of the MinION as we poured it into the chamber of our microdevice, this method is applicable in point-of-care-testing technology as a simple and high-throughput diagnostic system.

ASSOCIATED CONTENT

Supporting Information

The Supporting Information is available free of charge at https://pubs.acs.org/doi/10.1021/acs.analchem.3c02560.

Detailed information on experimental and data sampling/analysis; additional results of output duplexes formation; reference data preparation; estimation of the target specificity and concentration durability; and clinical-level operational confirmation of our proposed method (PDF)

AUTHOR INFORMATION

Corresponding Author

Ryuji Kawano − *Department of Biotechnology and Life Science, Graduate School of Engineering, Tokyo University of Agriculture and Technology, Tokyo 184-8588, Japan;*

https://doi.org/10.1021/acs.analchem.3c02560
Anal. Chem. XXXX, XXX, XXX−XXX

orcid.org/0000-0001-6523-0649; Email: rjkawano@cc.tuat.ac.jp

Authors

Sotaro Takiguchi − *Department of Biotechnology and Life Science, Graduate School of Engineering, Tokyo University of Agriculture and Technology, Tokyo 184-8588, Japan*

Fumika Kambara − *Department of Biotechnology and Life Science, Graduate School of Engineering, Tokyo University of Agriculture and Technology, Tokyo 184-8588, Japan*

Mika Tani − *Department of Maxillofacial Diagnostic and Surgical Science, Field of Oral and Maxillofacial Rehabilitation, Graduate School of Medical and Dental Science, Kagoshima University, Kagoshima 890-8544, Japan*

Tsuyoshi Sugiura − *Department of Maxillofacial Diagnostic and Surgical Science, Field of Oral and Maxillofacial Rehabilitation, Graduate School of Medical and Dental Science, Kagoshima University, Kagoshima 890-8544, Japan; Division of Oral and Maxillofacial Oncology and Surgical Sciences, Graduate School of Dentistry, Tohoku University, Miyagi 980-8577, Japan*

Complete contact information is available at: https://pubs.acs.org/10.1021/acs.analchem.3c02560

Author Contributions

S.T. and R.K. conceived the original idea. S.T. performed all experiments. F.K. and M.T. conducted experiments related to RT-qPCR, and T.S. and R.K. supervised the entire research. S.T. and R.K. wrote the entire manuscript, and all authors approved the final version of the manuscript.

Notes

The authors declare no competing financial interest.

■ ACKNOWLEDGMENTS

This research was partially supported by KAKENHI Grant Nos. 16H06043, 19H00901, 21H03143, 21H05229, and the WISE Program: Doctoral Program for World-leading Innovative & Smart Education of TUAT from MEXT, Japan. The authors thank A. Cooney for language editing.

■ REFERENCES

(1) Adleman, L. M. *Science* **1994**, *266*, 1021−1024.
(2) Braich, R. S.; Chelyapov, N.; Johnson, C.; Rothemund, P. W. K.; Adleman, L. *Science* **2002**, *296*, 499−502.
(3) Benenson, Y.; Paz-Elizur, T.; Adar, R.; Keinan, E.; Livneh, Z.; Shapiro, E. *Nature* **2001**, *414*, 430−434.
(4) Benenson, Y.; Adar, R.; Paz-Elizur, T.; Livneh, Z.; Shapiro, E. *Proc. Natl. Acad. Sci. U.S.A.* **2003**, *100*, 2191−2196.
(5) Seelig, G.; Soloveichik, D.; Zhang, D. Y.; Winfree, E. *Science* **2006**, *314*, 1585−1588.
(6) Stojanovic, M. N.; Mitchell, T. E.; Stefanovic, D. *J. Am. Chem. Soc.* **2002**, *124*, 3555−3561.
(7) Benenson, Y. *Mol. Biosyst.* **2009**, *5*, 675−685.
(8) Benenson, Y. *Nat. Rev. Genet.* **2012**, *13*, 455−468.
(9) Jung, C.; Ellington, A. D. *Acc. Chem. Res.* **2014**, *47*, 1825−1835.
(10) Kasianowicz, J. J.; Brandin, E.; Branton, D.; Deamer, D. W. *Proc. Natl. Acad. Sci. U.S.A.* **1996**, *93*, 13770−13773.
(11) Meller, A.; Nivon, L.; Brandin, E.; Golovchenko, J.; Branton, D. *Proc. Natl. Acad. Sci. U.S.A.* **2000**, *97*, 1079−1084.
(12) Branton, D.; Deamer, D. W.; Marziali, A.; Bayley, H.; Benner, S. A.; Butler, T.; Di Ventra, M.; Garaj, S.; Hibbs, A.; Huang, X. H.; Jovanovich, S. B.; Krstic, P. S.; Lindsay, S.; Ling, X. S. S.; Mastrangelo, C. H.; Meller, A.; Oliver, J. S.; Pershin, Y. V.; Ramsey, J. M.; Riehn, R.; Soni, G. V.; Tabard-Cossa, V.; Wanunu, M.; Wiggin, M.; Schloss, J. A. *Nat. Biotechnol.* **2008**, *26*, 1146−1153.
(13) Ding, T. L.; Yang, J.; Pan, V.; Zhao, N.; Lu, Z. H.; Ke, Y. G.; Zhang, C. *Nucleic Acids Res.* **2020**, *48*, 2791−2806.
(14) Perera, R. T.; Fleming, A. M.; Peterson, A. M.; Heemstra, J. M.; Burrows, C. J.; White, H. S. *Biophys. J.* **2016**, *110*, 306−314.
(15) Shim, J. W.; Tan, Q. L.; Gu, L. Q. *Nucleic Acids Res.* **2009**, *37*, 972−982.
(16) Kawano, R. *Biotechnol. J.* **2018**, *13*, No. 1800091.
(17) Yasuga, H.; Kawano, R.; Takinoue, M.; Tsuji, Y.; Osaki, T.; Kamiya, K.; Miki, N.; Takeuchi, S. *PLoS One* **2016**, *11*, No. e0149667.
(18) Yasuga, H.; Inoue, K.; Kawano, R.; Takinoue, M.; Osaki, T.; Kamiya, K.; Miki, N.; Takeuchi, S. *PLoS One* **2017**, *12*, No. e0180876.
(19) Ohara, M.; Takinoue, M.; Kawano, R. *ACS Synth. Biol.* **2017**, *6*, 1427−1432.
(20) Takiguchi, S.; Kawano, R. *Nanoscale* **2021**, *13*, 6192−6200.
(21) Bartel, D. P. *Cell* **2004**, *116*, 281−297.
(22) Esquela-Kerscher, A.; Slack, F. J. *Nat. Rev. Cancer* **2006**, *6*, 259−269.
(23) Hiratani, M.; Kawano, R. *Anal. Chem.* **2018**, *90*, 8531−8537.
(24) Chen, L.; Yan, H. X.; Yang, W.; Hu, L.; Yu, L. X.; Liu, Q.; Li, L.; Huang, D. D.; Ding, J.; Shen, F.; Zhou, W. P.; Wu, M. C.; Wang, H. Y. *J. Hepatol.* **2009**, *50*, 358−369.
(25) Takeuchi, N.; Hiratani, M.; Kawano, R. *JACS Au* **2022**, *2*, 1829−1838.
(26) Siegel, R. L.; Miller, K. D.; Jemal, A. *Ca-Cancer J. Clin.* **2015**, *65*, 5−29.
(27) Miyagi, M.; Takiguchi, S.; Hakamada, K.; Yohda, M.; Kawano, R. *Proteomics* **2022**, *22*, No. e2100070.
(28) Liu, P.; Kawano, R. *Small Methods* **2020**, *4*, No. 2000101.
(29) Nakamura, K.; Hiyake, N.; Hamada, T.; Yokoyama, S.; Mori, K.; Yamashiro, K.; Beppu, M.; Sagara, Y.; Sagara, Y.; Sugiura, T. *Cancers* **2021**, *13*, 449.
(30) Henrickson, S. E.; Misakian, M.; Robertson, B.; Kasianowicz, J. J. *Phys. Rev. Lett.* **2000**, *85*, 3057−3060.
(31) Wang, Y.; Zheng, D. L.; Tan, Q. L.; Wang, M. X.; Gu, L. Q. *Nat. Nanotechnol.* **2011**, *6*, 668−674.
(32) Vercoutere, W.; Winters-Hilt, S.; Olsen, H.; Deamer, D.; Haussler, D.; Akeson, M. *Nat. Biotechnol.* **2001**, *19*, 248−252.
(33) Arias-Gonzalez, J. R. *Integr. Biol.* **2014**, *6*, 904−925.
(34) Wahlestedt, C.; Salmi, P.; Good, L.; Kela, J.; Johnsson, T.; Hokfelt, T.; Broberger, C.; Porreca, F.; Lai, J.; Ren, K. K.; Ossipov, M.; Koshkin, A.; Jakobsen, N.; Skouv, J.; Oerum, H.; Jacobsen, M. H.; Wengel, J. *Proc. Natl. Acad. Sci. U.S.A.* **2000**, *97*, 5633−5638.
(35) Petersen, M.; Bondensgaard, K.; Wengel, J.; Jacobsen, J. P. *J. Am. Chem. Soc.* **2002**, *124*, 5974−5982.
(36) Xi, D. M.; Shang, J. Z.; Fang, E. G.; You, J. M.; Zhang, S. S.; Wang, H. *Anal. Chem.* **2016**, *88*, 10540−10546.
(37) Lei, J.; Huang, Y. Q.; Zhong, W. J.; Xiao, D.; Zhou, C. S. *Anal. Chem.* **2020**, *92*, 8867−8873.
(38) Kozomara, A.; Birgaoanu, M.; Griffiths-Jones, S. *Nucleic Acids Res.* **2019**, *47*, D155−D162.
(39) Wang, Y.; Tian, K.; Hunter, L. L.; Ritzo, B.; Gu, L. Q. *Nanoscale* **2014**, *6*, 11372−11379.
(40) Ivanova, A.; Rosch, N. *J. Phys. Chem. A* **2007**, *111*, 9307−9319.
(41) Mitchell, N.; Howorka, S. *Angew. Chem., Int. Ed.* **2008**, *47*, 5565−5568.
(42) Zhang, H. L.; Hiratani, M.; Nagaoka, K.; Kawano, R. *Nanoscale* **2017**, *9*, 16124−16127.
(43) Yeung, W. K.; Chen, H. Y.; Sun, J. J.; Hsieh, T. H.; Mousavi, M. Z.; Chen, H. H.; Lee, K. L.; Lin, H.; Wei, P. K.; Cheng, J. Y. *Analyst* **2018**, *143*, 4715−4722.
(44) Azzouzi, S.; Fredj, Z.; Turner, A. P. F.; Ben Ali, M.; Mak, W. C. *ACS Sens.* **2019**, *4*, 326−334.
(45) Rondelez, Y.; Gines, G. *ACS Sens.* **2020**, *5*, 2430−2437.
(46) Jain, M.; Olsen, H. E.; Paten, B.; Akeson, M. *Genome Biol.* **2016**, *17*, 239.
(47) Kang, A. S. W.; Bernasconi, J. G.; Jack, W.; Kanavarioti, A. *Sci. Rep.* **2020**, *10*, No. 19790.

(48) Cardozo, N.; Zhang, K. R.; Doroschak, K.; Nguyen, A.; Siddiqui, Z.; Bogard, N.; Strauss, K.; Ceze, L.; Nivala, J. *Nat. Biotechnol.* **2022**, *40*, 42−46.
(49) Zhang, K. R.; Chen, Y. J.; Wilde, D.; Doroschak, K.; Strauss, K.; Ceze, L.; Seelig, G.; Nivala, J. *Nat. Commun.* **2022**, *13*, No. 4904.

https://doi.org/10.1021/acs.analchem.3c02560
Anal. Chem. XXXX, XXX, XXX−XXX